Analysis of the fine structure of Sn^{11+}–Sn^{14+} ions by optical spectroscopy in an electron-beam ion trap

A. Windberger,[1,2] F. Torretti,[1,3] A. Borschevsky,[4] A. Ryabtsev,[5,6] S. Dobrodey,[2] H. Bekker,[2] E. Eliav,[7] U. Kaldor,[7] W. Ubachs,[1,3] R. Hoekstra,[1,8] J. R. Crespo López-Urrutia,[2] and O. O. Versolato[1,*]

[1]*Advanced Research Center for Nanolithography, Science Park 110, 1098 XG Amsterdam, The Netherlands*

[2]*Max-Planck-Institut für Kernphysik, Saupfercheckweg 1, 69117 Heidelberg, Germany*

[3]*Department of Physics and Astronomy, and LaserLaB, Vrije Universiteit, De Boelelaan 1081, 1081 HV Amsterdam, The Netherlands*

[4]*Van Swinderen Institute, University of Groningen, Nijenborgh 4, 9747 AG Groningen, The Netherlands*

[5]*Institute of Spectroscopy, Russian Academy of Sciences, Troitsk, Moscow, 108840, Russia*

[6]*EUV Labs, Ltd., Troitsk, Moscow, 108840, Russia*

[7]*School of Chemistry, Tel Aviv University, 69978 Tel Aviv, Israel*

[8]*Zernike Institute for Advanced Materials, University of Groningen, Nijenborgh 4, 9747 AG Groningen, The Netherlands*

(Received 4 May 2016; published 7 July 2016)

We experimentally re-evaluate the fine structure of Sn^{11+}–Sn^{14+} ions. These ions are essential in bright extreme-ultraviolet (EUV) plasma-light sources for next-generation nanolithography, but their complex electronic structure is an open challenge for both theory and experiment. We combine optical spectroscopy of magnetic dipole $M1$ transitions, in a wavelength range covering 260 to 780 nm, with charge-state selective ionization in an electron beam ion trap. Our measurements confirm the predictive power of *ab initio* calculations based on Fock space coupled cluster theory. We validate our line identification using semiempirical COWAN calculations with adjustable wave-function parameters. Available Ritz combinations further strengthen our analysis. Comparison with previous work suggests that line identifications in the EUV need to be revisited.

DOI: 10.1103/PhysRevA.94.012506

I. INTRODUCTION

The strongly correlated electronic structure of heavy, multielectron open shell ions is notoriously difficult to calculate and their complicated structure furthermore hampers straightforward experimental assessment. A typical example of this class of systems are Sn ions in charge states 7+ through 14+ with their open [Kr]4d shell structure. These specific ions are used to generate extreme ultraviolet (EUV) light at 13.5-nm wavelength in laser-produced-plasma (LPP) sources for nanolithographic applications [1,2]. The EUV light is generated by thousands of transitions that form so-called unresolved transition arrays (UTAs) with little dependence on the charge state of the ion. For the relevant [Kr]$4d^m$ tin ions, with $m = 6$–0 [3], the EUV-contributing upper configurations are $4p^6\,4d^{m-1}\,4f^1$,$4p^6\,4d^{m-1}5p^1$, and $4p^5\,4d^{m+1}$. The sheer multitude of lines in these UTAs complicates their accurate identification. Spectroscopic work using discharge sources [4–9], laser-produced-plasmas [10], or tokamaks [11,12] is challenging as the UTAs of various Sn ions are strongly blended. Nevertheless, work on discharge sources provides the most accurate spectroscopic data to date for highly charged Sn ions.

Besides experiments on thermal plasmas, there is work on charge state-resolved spectroscopy in the EUV regime. Charge-exchange spectroscopy (CXS) was performed by means of Sn ion beams colliding on He [13–16] and Xe [16] gas targets. The spectral accuracy achieved in those studies was lower than that of the discharge work due to instrument resolution. Studies using electron beam ion traps (EBITs) [13,17] which also provide charge state selectivity were similarly limited. In addition, the EBIT studies focused on the higher charge states of tin, outside of the range most relevant for EUV plasma sources. For these reasons, none of the charge-state-resolved studies could so far directly challenge the spectral data obtained from discharge sources.

The above issues of unresolved transitions in UTAs and limited resolution can be circumvented by turning to the optical range and addressing the optical magnetic dipole ($M1$) transitions between fine structure levels in the ground electronic configuration (see Fig. 1). This approach eliminates the uncertainties introduced by the reconstruction of ground-state levels using a Ritz procedure based on the measured EUV lines. Such optical lines of Sn in charge states beyond 3+ have not been identified before.

We present results from charge-state-resolved optical spectroscopy on Sn^{11+}–Sn^{14+} using FLASH-EBIT [19] at the Max Planck Institute for Nuclear Physics in Heidelberg. Tuning the energy of the electron beam enables us to assign each of the observed spectral lines to specific charge states. The $M1$ transitions are assigned using *ab initio* Fock space coupled cluster (FSCC) [20,21] calculations and we confirm them with the help of the semi-empirical COWAN code [22], which allows adjusting wave-function scaling parameters to fit the observed spectra.

Optical transitions in heavy multielectron open shell ions like Sn^{11+}–Sn^{14+} represent a stringent test for *ab initio* atomic structure calculations of strongly correlated many-electron ions. These transitions have non-negligible Breit contributions. Application of FSCC theory to this type of problems where multiple vacancies with high angular momenta can couple to each other is a promising approach. Coupled cluster methods have found wide application since the 1950s to analogous problems found in nuclear physics and quantum chemistry, yet their use for atomic physics problems involving highly charged ions is more recent (see, e.g., Ref. [23]).

*o.versolato@arcnl.nl

 ©2016 American Physical Society

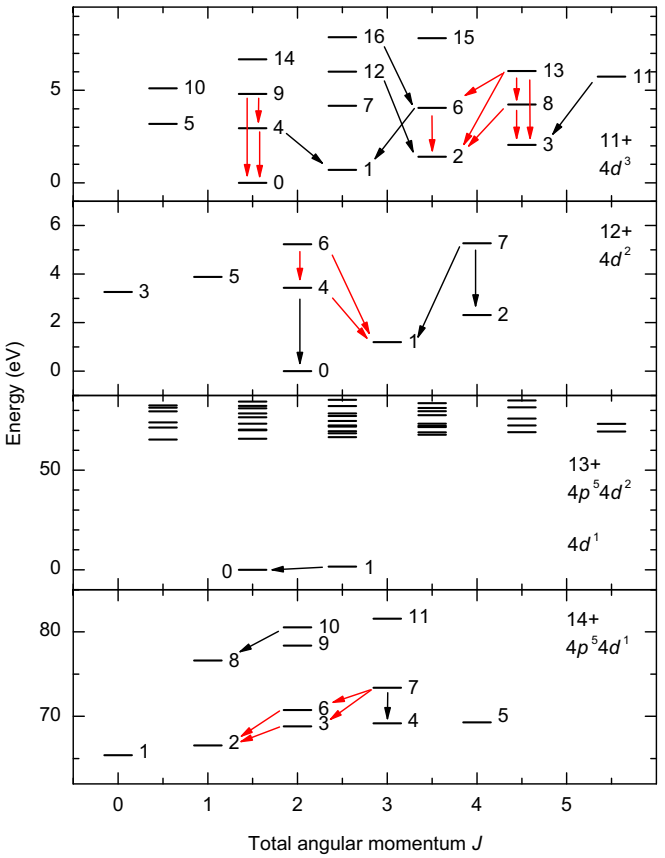

FIG. 1. Grotrian diagrams obtained from FLEXIBLE ATOMIC CODE calculations [18] depicting the atomic structure of the lowest energy configurations exhibiting optical magnetic dipole $M1$ transitions of the Sn charge states investigated in this work. The closed-shell [Kr] ground state of Sn^{14+} has no splitting; instead the first excited configuration is shown. The levels are numbered following their energy ordering. Their respective term symbols can be found in Table III. Identified transitions are marked by arrows: red, transitions confirmed by Ritz combinations; black, the remainder. All observed spectral lines and identified transitions are listed in Table I.

There are only few such works so far, although the methods consistently show good agreement with experiments (see, e.g., Refs. [24–27]). It is therefore instructive to explore their *ab initio* performance in specific cases where other established calculational tools require empirical adjustments and judicious choices of configuration sets in order to analyze spectral data. Therefore, with optical spectroscopic studies we can address the issue of a precise theory-experiment comparison in complex open-shell systems without the high spectral density that has to be faced in EUV spectroscopy work. In the present case, both the important practical applications of the ions under study as well as the relative novelty of using FSCC calculations for them make such a comparison particularly valuable.

Our data enable a re-evaluation of the fine structure splitting of Sn^{11+}–Sn^{14+} ions and provide a benchmark for state-of-the-art atomic structure calculations such as FSCC. We infer that the identification of EUV lines needs to be revisited in previous works such as Ref. [7,9], as was also suggested previously in Ref. [28]. The line identifications in those works constitute the basis for plasma modeling of EUV light sources.

II. EXPERIMENT

We produced and trapped Sn ions with FLASH-EBIT [19] using a monoenergetic electron beam to bring them to the desired charge state. The beam energy was controlled by the acceleration potential applied between the emitting cathode and the central trap drift tube. High current densities were reached by compressing the electron beam down to a diameter of approximately 50 μm using the 6-T magnetic field produced by a pair of superconducting Helmholtz coils. A tenuous, well-collimated molecular beam generated by the evaporation of volatile tetra-i-propyltin ($C_{12}H_{28}Sn$) was the carrier of Sn atoms into the electron beam, which dissociated the molecule and preferentially trapped the heavy Sn ions thereby produced. While the lighter atoms and ions of C and H escaped from the trap, Sn ions remained trapped, radially by the space charge potential of the electron beam and axially by a potential generated by a set of drift tubes.

The trapped ions were electronically excited by electron impact to a manifold of states, many of them close to the ionization continuum since the beam energy is close to the respective ionization threshold. Subsequent fluorescent cascades down towards the ground state cover a broad spectral range. This light was focused onto the entrance slit of a 320-mm-focal-length spectrometer employing a 300 lines/mm grating. We use in this work a low groove density grating and a short focal distance instrument for the convenience of having a broad spectral coverage, given the large number of spectra to be acquired. The spectral image recorded by a cooled CCD is integrated along the nondispersive axis after correcting for optical aberrations and removing cosmic muon events. Line widths of typically ~1 nm (full-width-at-half-maximum) were obtained near 400-nm wavelength. For calibration a Hg or a Ne-Ar lamp was placed in front of the spectrometer entrance slit.

A typical acquisition cycle consisted of a short calibration and a series of 30-min exposures. After each acquisition the electron beam acceleration potential was increased by 10 V starting from a minimum acceleration potential of 137 V and ending at 477 V. The electron beam current was kept at a constant 10 mA. The dense electron beam produces a strong space charge potential which is partially compensated by the trapped ions [29,30]. This reduces the acceleration potential by ~20–40 V [31] to yield the actual electron beam energy in the interaction region. The chosen range of the acceleration potential enabled the production of charge states from Sn^{7+}, with its ionization potential (V_{ion}) of 135 V [32,33] up to Sn^{16+} with $V_{ion} = 437$ V. We focus on the charge states Sn^{11+}–Sn^{14+} that could be reliably identified.

After stepping the EBIT acceleration potential through the full voltage range, the rotatable grating was set to cover a 125-nm adjacent wavelength range. Typically, a range of 270 nm was recorded at each grating position, so that the different regions overlapped. Next, the acceleration potential was stepped through again. This procedure was repeated for three settings of the spectrometer grating to cover the full accessible wavelength range from 260 to 780 nm.

III. THEORY

Two calculational methods are compared in this work. First, we present dedicated *ab initio* FSCC calculations and show

the accuracy of these predictions by comparison with our experimental data. Second, we compare them with COWAN code calculations using empirically adjusted wave-function scaling parameters. This code is a mature tool used to identify lines and serves particularly well when a combination of experimental observations provides additional data on electronic energy levels for their empirical adjustment. We also use it to obtain weighted transition rates gA used to predict line strengths. When necessary, auxiliary calculations were carried out with the FLEXIBLE ATOMIC CODE (FAC) [18].

A. Fock-space-coupled cluster

Calculations of the transition energies were performed for the ions of interest using the FSCC method within the framework of the projected Dirac-Coulomb-Breit Hamiltonian [34],

$$H_{DCB} = \sum_i h_D(i) + \sum_{i<j}(1/r_{ij} + B_{ij}). \quad (1)$$

Here, $h_D(i)$ is the one-electron Dirac Hamiltonian,

$$h_D(i) = c\boldsymbol{\alpha}_i \cdot \mathbf{p}_i + c^2\beta_i + V_{\rm nuc}(i), \quad (2)$$

where $\boldsymbol{\alpha}$ and β are the four-dimensional Dirac matrices. The nuclear potential $V_{\rm nuc}(i)$ takes into account the finite size of the nucleus, modeled by a uniformly charged sphere [35]. The two-electron term includes the nonrelativistic electron repulsion and the frequency independent Breit operator,

$$B_{ij} = -\frac{1}{2r_{ij}}\left[\boldsymbol{\alpha}_i \cdot \boldsymbol{\alpha}_j + (\boldsymbol{\alpha}_i \cdot \mathbf{r}_{ij})(\boldsymbol{\alpha}_j \cdot \mathbf{r}_{ij})/r_{ij}^2\right], \quad (3)$$

and is correct to second order in the fine structure constant. The calculations for Sn^{14+},Sn^{13+}, and Sn^{12+} started from the closed-shell reference $4s^2 4p^6$ configuration of Sn^{14+}. In the current state of the code, atomic systems with a maximum of two open-shell electrons or holes can be treated, which does not apply to Sn^{11+} with its $4s^2\,4p^6\,4d^3$ ground-state configuration. After the first stage of the calculation, consisting of solving the relativistic Hartree-Fock equations and correlating the closed-shell reference state, different FSCC schemes were used for the different ions. In case of Sn^{14+}, a single electron was excited from the $4p$ to the $4d$ orbital to reach the $4p^5\,4d^1$ configuration. For Sn^{12+}, two electrons were added to the closed-shell reference state. In this calculation, to achieve optimal accuracy, a large model space was used, composed of three s, three p, three d, three f, two g, and one h orbitals. The intermediate Hamiltonian method was employed to facilitate convergence [36]. The fine structure splitting of Sn^{13+} was also obtained in the framework of this calculation, as a result of adding the first electron to the closed-shell reference state.

The uncontracted universal basis set [37] was used for all the ions, consisting of 37 s, 31 p, 26 d, 21 f, 16 g, 11 h, and six i functions; the convergence of the obtained transition energies with respect to the size of the basis set was verified. All the electrons were correlated. The FSCC calculations were performed using the TEL AVIV RELATIVISTIC ATOMIC FSCC code (TRAFS-3C) [38].

Lamb shifts for the various levels were obtained using the recently developed effective potential method, implemented in the QEDMOD program [39]. Here, an important feature

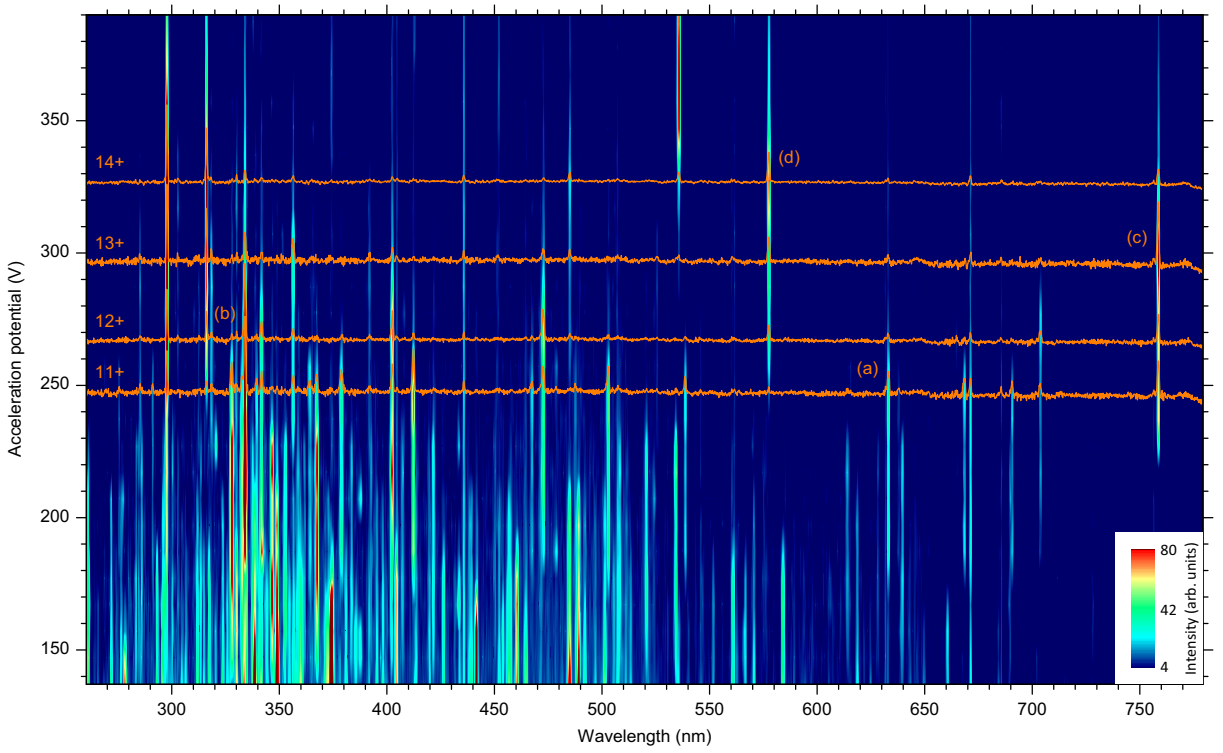

FIG. 2. Composite spectral map of Sn ions interpolated between discrete voltage steps of the EBIT acceleration potential at a 10-mA beam current. The orange curves represent spectra of Sn^{11+}–Sn^{14+} ions taken at a maximum of the fluorescence yield of a specific charge state; they are individually scaled for better visibility. Enlarged sections around the lines indicated by symbols (a), (b), (c), and (d) can be found in Fig. 3 to visualize the identification of charge states through their fluorescence profiles.

is the inclusion of both the vacuum polarization and the self-energy components of the Lamb shift into the self-consistent field procedure. Thus, together with the first-order QED interactions, many important higher order terms are included in the final Lamb shift expression. Its contribution to level energies is typically 20–60 cm^{-1}. The results of the calculations are presented in Table III, where they are compared to the experimental results, as will be discussed in the next section.

B. COWAN

In the COWAN code [22], radial wave functions are obtained with a Hartree-Fock relativistic (HFR) method using a correlation term in the potential but accounting for the Breit interaction only partially. With these wave functions, the electrostatic single configuration radial integrals F^k and G^k (Slater integrals), configuration-interaction Coulomb radial integrals, and spin-orbit parameters ζ are then calculated. From these, the energy levels and intermediate coupling eigenvectors are extracted. Subsequently, *ab initio* values are obtained for the wavelengths and transition probabilities. However, the resulting energy level splittings are generally larger than those observed because of the cumulative influence of a large number of small perturbations originating from configuration interactions. To compensate for these effects the *ab initio* values of the electrostatic integrals are empirically scaled down by a factor between 0.7 and 0.95, depending on the charge state. Spin-orbit parameters can also be scaled. Both scalings are needed for a semi-empirical adjustment of the predicted spectrum that can be performed if enough experimental levels are available. The electrostatic and spin-orbit integrals are then adjusted to give the best possible fit of the calculated eigenvalues to the observed energy levels. Effective Coulomb-interaction operators α, β, and $T1$ are added as fit parameters to represent weak configuration-interaction corrections to the electrostatic single configuration effects. The results of this semiempirical adjustment procedure are more useful for the interpretation of a particular experimental spectrum than the *ab initio* COWAN calculation. Additionally, the empirical ratios of the fitted (FIT) to the HFR energy parameters can be extrapolated, e.g., to neighboring ions along an isoelectronic sequence to improve the reliability of *ab initio* predictions.

IV. RESULTS

In the following, we present optical spectra of tin ions in charge states Sn^{11+}–Sn^{14+} obtained in a charge-state-resolved manner (see Figs. 2 and 3). We interpret the data using FSCC

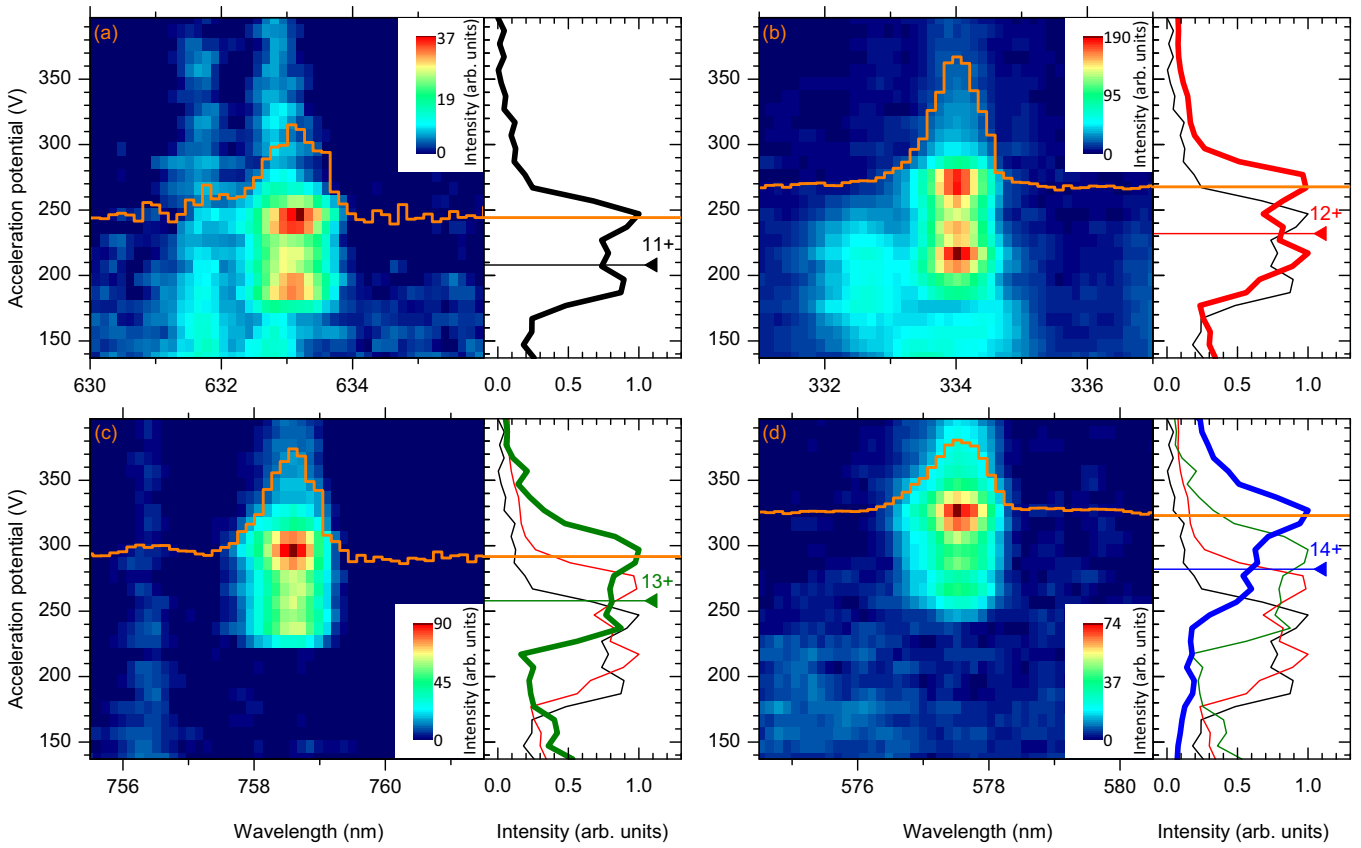

FIG. 3. Enlarged sections around the spectral lines marked (a), (b), (c), and (d) in Fig. 2 assigned to the charge states Sn^{11+}, Sn^{12+}, Sn^{13+}, and Sn^{14+}. On the right-hand side of the composite spectral maps we show the respective projection onto the acceleration potential axis as black (Sn^{11+}), red (Sn^{12+}), green (Sn^{13+}), and blue (Sn^{14+}) curves. Theoretical ionization energies of the charge states [32,33] are depicted by triangles and colored accordingly. The profiles were averaged over several bright spectral lines exhibiting the same voltage dependence. By combining the obtained profiles, as shown in panel (d), a ladder was constructed which enabled the charge state identification of spectral lines (see main text). The overlaid orange spectra (also see Fig. 2) are obtained at the acceleration potential that maximizes the fluorescence yield.

TABLE I. Vacuum wavelengths and relative intensities for spectral lines of Sn^{11+}–Sn^{14+} ions measured at the EBIT acceleration potential V_{max} that yielded maximum fluorescence. The experimental wavelength uncertainty of ∼0.4 nm is mainly due to the uncertainty in the calibration. All observed lines could be identified for Sn^{11}, Sn^{12}, and Sn^{14+}. Our identifications were further confirmed with Ritz combinations where available (see Fig. 1); lines involved in Ritz combination groups are indicated by the superscript letters a, b, c, d, e, and f. Lines near 328- and 368-nm wavelengths, now associated with Sn^{10+}, show signs of weak, blended contributions of Sn^{11+}, but their unambiguous identification is left for future work. Intensities were derived from the total area of the Gaussian fit, and were corrected for the grating efficiency. Theoretical wavelengths λ_{FSCC} were obtained from FSCC. Wavelengths obtained from semiempirical COWAN code calculations are marked λ_{COWAN} and the associated weighted transition rates $gA_{ij,COWAN}$ are given. "Transition" gives lower and upper states contributing to transition (from Fig. 1), with their respective configuration and (approximate) term given in the last two columns.

Ion	V_{max} (V)	λ_{exp} (nm)	Intensity (arb. units)	λ_{FSCC} (nm)	λ_{COWAN} (nm)	$gA_{ij,COWAN}$ (s^{-1})	Transition (see Fig. 1)	Configuration	Term symbol
11+	247	275.6[a]	8		276	102	0–9	[Kr]$4d^3$	$^4F_{3/2}$–$^2D_{3/2}$
		291.2[b,c]	14		292	100	2–13		$^4F_{7/2}$–$^2G_{9/2}$
		297.8	23		297	308	2–12		$^4F_{7/2}$–$^2D_{5/2}$
		339.5[d]	34		341	79	3–13		$^4F_{9/2}$–$^2G_{9/2}$
		364.2	44		365	48	6–16		$^2G_{7/2}$–$^2F_{5/2}$
		378.9	81		379	59	3–11		$^4F_{9/2}$–$^2H_{11/2}$
		412.4	136		412	253	1–6		$^4F_{5/2}$–$^2G_{7/2}$
		467.5[a]	39		468	55	0–4		$^4F_{3/2}$–$^4P_{3/2}$
		503.0[c]	129		503	165	2–8		$^4F_{7/2}$–$^2H_{9/2}$
		538.7[b]	75		539	125	2–6		$^4F_{7/2}$–$^2G_{7/2}$
		633.3[b]	178		637	268	6–13		$^2G_{7/2}$–$^2G_{9/2}$
		638.1	53		640	17	1–4		$^4F_{5/2}$–$^4P_{3/2}$
		668.5[d]	143		668	211	3–8		$^4F_{9/2}$–$^2H_{9/2}$
		671.5[a]	51		674	139	4–9		$^4P_{3/2}$–$^2D_{3/2}$
		690.7[c,d]	92		695	267	8–13		$^2H_{9/2}$–$^2G_{9/2}$
12+	267	334.1	247	337	334	290	1–7	[Kr]$4d^2$	$^3F_3$–$^1G_4$
		341.8[e]	65	335	342	87	1–6		$^3F_3$–$^3P_2$
		402.6	122	396	402	117	0–4		$^3F_2$–$^1D_2$
		472.7	185	478	471	162	2–7		$^3F_4$–$^1G_4$
		665.0[e]	63	643	658	36	1–4		$^3F_3$–$^1D_2$
		703.9[e]	167	698	712	151	4–6		$^1D_2$–$^3P_2$
13+	297	285.2	11						
		318.5	19						
		356.5	62						
		391.9	17						
		525.6	24						
		758.8	518	763	757	150	0–1	[Kr]$4d^1$	$^2D_{3/2}$–$^2D_{5/2}$
14+	327	297.9[f]	211	292	295	984	3–7	$4p^5\ 4d^1$	$^3P_2$–$^3D_3$
		302.9	15	308	302	2597	8–10		$^3D_1$–$^3D_2$
		316.3	109	308	311	516	4–7		$^3F_3$–$^3D_3$
		330.2[f]	20	331	319	62	2–6		$^3P_1$–$^1D_2$
		485.1[f]	51	465	503	80	6–7		$^1D_2$–$^3D_3$
		577.7[f]	207	571	575	349	2–3		$^3P_1$–$^3P_2$

predictions and semiempirical COWAN code calculations. Furthermore, we perform a comparison with predicted optical transition energies inferred from existing data in the EUV regime. We discuss first the charge state identification and second the line identifications. All results are summarized in Tables I, II, and III.

A. Charge-state identification

Scanning the electron beam energy enables the assignment of lines to specific charge states (see Refs. [31,40] and references therein), although the absolute determination of a charge number can be challenging (see, e.g., Ref. [41]). A typical characteristic of EBIT spectra is that groups of spectral lines that exhibit the same dependence on the acceleration potential can be assigned to the same charge state (see Fig. 2). The appearance and disappearance of sets of lines enables the construction of a so-called ladder of charge states (see Fig. 3). The challenge remaining is to pinpoint a single charge state, with which the others would be easily identified counting up and down. For this purpose, we used the fact that the [Kr]$4d^1$ ground-state configuration of Sn^{13+} allows for only a single optical transition originating from the $4d^2\,D_{3/2}$–$^2D_{5/2}$ fine structure splitting (see Fig. 1). This transition is predicted by FSCC to occur near 13 144 cm^{-1} (see Table III), in agreement with the 13 212(25) cm^{-1} obtained from the EUV spectra in Refs. [7,8]. The brightest line, observed at 758.8(4) nm wavelength or 13 179(8) cm^{-1}, is an excellent match for it.

TABLE II. COWAN code Hartree-Fock (HFR) and fitted (FIT) parameters (with uncertainties δ_{fit}), their ratios (scaling factors), and root mean square deviations σ of the fits as calculated for the $4d^k + 4d^{k-1}5s + 4d^{k-2}5s^2$ interacting configurations ($k = 3,2$ respectively in the Sn^{11+} and Sn^{12+} spectra). The electrostatic parameters were scaled by a factor 0.85 whereas average energies and spin-orbit parameters were not scaled in the unknown $4d^{k-1}5s$ and $4d^{k-2}5s^2$ configurations. All parameters are given in units of cm^{-1}.

	Sn^{11+}				Sn^{12+}			
Parameter	HFR	FIT	δ_{fit}	FIT/HFR	HFR	FIT	δ_{fit}	FIT/HFR
E_{av}	41 025	37 533	17		26 035	24 435	2	
$F^2(4d,4d)$	114 058	97 715	121	0.857	116 377	99 790	21	0.857
$F^4(4d,4d)$	76 975	68 047	323	0.884	78 692	69 026	270	0.877
α		64	3			68	1	
β		−600	Fixed			−600	Fixed	
$T1$		−4.4	Fixed					
$\zeta(4d)$	4 638	4 774	16	1.029	4 868	5 028	2	1.033
σ		57				4		

This unambiguously fixes the identification of Sn^{13+} and with it, that of the other charge states (see Fig. 3).

The onsets of fluorescence for all identified charge states occurred at lower acceleration potentials than expected from theory [32,33], as is depicted in Fig. 3. This, together with the shape of the fluorescence curves, indicates strong contributions from metastable states [42]. The doubly peaked structure observed for all four charge states hints at metastable states at an excitation energy of ∼60 eV. This excitation energy is similar to that of the low-lying high-J levels of the first excited configuration $4p^5\,4d^{m+1}$ that are metastable for decay through electric dipole $E1$ transitions. The observed dependence of the fluorescence of a particular charge state Sn^{11+}–Sn^{14+} on the electron beam energy can be qualitatively understood by the sequential opening of four different channels (see Fig. 4). Such strong contributions from metastable states are of particular interest for plasma modeling.

A few spectral lines could not be linked to a specific Sn ion. These lines turned out to have only a weak dependence on the electron beam energy. They originate most likely from residual gas or W or Ba ions stemming from the cathode as they remained visible without Sn injection.

B. Line identification

The wavelengths and intensities of the spectral lines for each identified charge state were extracted at the acceleration potential that maximized its fluorescence intensity (see Figs. 3 and 5). Listed in Table I are the centers of the lines, as obtained by fitting Gaussian functions to them. The uncertainty in the determination of the transition wavelengths is dominated by the uncertainty in the spectrometer calibration. Due to a relatively weak signal, the Sn^{11+}–Sn^{14+} spectra were acquired using a wider entrance slit than needed for the calibration source to reach a sufficient fluorescence intensity. This enlarged the influence of any minor misalignments of the two light paths, resulting in a systematic uncertainty estimated at ∼0.4 nm. We obtained this uncertainty by comparing spectral lines in the overlap region of different wavelength ranges. Also listed are the signal intensities given by the area under the fitted Gaussian curves, corrected for the spectral grating efficiency. The accuracy of this procedure is limited, and uncertainties in the determination of the total signal are further introduced by chromatic aberrations of the coupling optics, the finite aperture width, and polarization effects. However, this accuracy should be higher when comparing the relative intensities of transitions with close-lying wavelengths.

Accurate, experimentally obtained spectra in the EUV regime are available for the charge states Sn^{7+} [6], Sn^{8+}–Sn^{11+} [9], Sn^{13+} [8], and $Sn^{12,13,14+}$ [7]. Transitions in the higher charge states were measured by D'Arcy and coworkers [14,15]. We focus our discussion on the charge states Sn^{11+}–Sn^{14+}. As pointed out previously [28], the identification of weak EUV lines needs to be corrected in previous works. Nevertheless, we will start out by comparing our results to the reference data as is, except in the case of Sn^{12+} for which a new interpretation based on existing EUV spectral data is presented here. Further, a direct comparison is made to the FSCC calculations. In the following the results per charge state are discussed in detail.

1. Sn^{11+}

First identifications of transitions within the $[Kr]4d^3$ ground state were obtained from a comparison of the observed energies to the transition energies resulting from the semi-empirical COWAN energy parameters as obtained from Ref. [9]. We associated the predicted transitions of high gA values with the closest-lying, brightest spectral lines (see Fig. 5). In this manner, enough levels were identified to enable a fit of the calculations to these levels, improving on the original predictions. This in turn enabled the further identification of observed lines. Iterating the above procedure, all lines attributed to the Sn^{11+} spectrum were identified (see Table I). In the final step, the obtained energies of the levels were optimized employing Kramida's code LOPT (for level optimization) [43]. The energy levels thus derived from the experimental wavelengths are collected in Table III. A comparison of the energy parameters is presented in Table II: on the one hand, those obtained from *ab initio* HFR calculations, and on the other hand, those obtained from fitting the COWAN code to the experimental level values obtained from LOPT. The effective parameters β and $T1$ were fixed in the fitting on the values roughly estimated from the isoelectronic spectrum of Pd^{7+} [44] and the isonuclear spectrum of Sn^{7+} [4].

TABLE III. Energy levels E_{exp} (all energies in cm^{-1}) derived from the experimental data using Kramida's LOPT algorithm [43], *ab initio* FSCC calculations E_{FSCC} (including individual contributions from the Breit interaction ΔE_{Breit} and Lamb shift ΔE_{LS}), as well as semiempirical COWAN code calculations E_{COWAN} of the investigated fine-structure configurations in Sn^{11+}–Sn^{14+}. Levels (from Fig. 1) are ordered by their energies; we use *LS*-term notations as approximated from the COWAN code. The dispersive energy uncertainty D_1 is close to the minimum uncertainty of separation from other levels, and the energy uncertainty D_2 is that relative to the ground level (or to the $^3P_1$ level in Sn^{14+} which is offset to zero E_{FSCC} and E_{COWAN} in this table; ΔE_{Breit} and ΔE_{LS} are given with respect to the ground level $^1S_0$); see the exact definition in Ref. [43]. The number of spectral lines used for the determination of each level energy is given by N. Semiempirical COWAN code calculations are given in column E_{COWAN}. The identification of spectral lines in Sn^{11+} and Sn^{12+} used an iterative fit procedure based on the measured spectra (see Sec. III B, Table II); for Sn^{13+} the value for E_{COWAN} was obtained from a single configuration HFR; and for Sn^{14+} the ratio FIT/HFR of COWAN parameters was determined by isoelectronic extrapolations and data from Ref. [11] (see main text). Energies deduced from vacuum-spark EUV spectra E_{vs} have uncertainties of ∼40 cm^{-1} [7,9]. The difference $\Delta E_{vs} = E_{exp} - E_{vs}$ of that interpretation with our own identifications suggests the need for revision of those earlier identifications.

			Experiment				FSCC					
Ion	Level	Term	E_{exp}	D_1	D_2	N	ΔE_{Breit}	ΔE_{LS}	E_{FSCC}	E_{COWAN}	E_{vs}	ΔE_{vs}
$11+\ 4d^3$	0	$^4F_{3/2}$	0	17	0	2				0	0	0
	1	$^4F_{5/2}$	5 719	9	20	2				5 758	5 760	−36
	2	$^4F_{7/2}$	11 403	10	30	3				11 445	11 465	−57
	3	$^4F_{9/2}$	16 321	9	30	2				16 375	16 390	−64
	4	$^4P_{3/2}$	21 391	6	17	3				21 390	20 486	905
	5	$^4P_{1/2}$								23 341		
	6	$^2G_{7/2}$	29 967	8	30	3				30 011	30 057	−84
	7	$^4P_{5/2}$								31 130		
	8	$^2H_{9/2}$	31 280	6	30	3				31 337	31 110	175
	9	$^2D_{3/2}$	36 283	9	19	2				36 216	35 810	471
	10	$^4P_{1/2}$								38 736		
	11	$^2H_{11/2}$	42 713	28	44	1				42 726	42 230	488
	12	$^2D_{5/2}$	44 983	45	56	1				45 081	44 990	−2
	13	$^2G_{9/2}$	45 759	6	30	4				45 720	45 705	59
	14	$^2P_{3/2}$								51 365		
	15	$^2F_{7/2}$								57 261	55 460	
	16	$^2F_{5/2}$	57 425	30	43	1				57 414	55 660	1 770
$12+\ 4d^2$	0	$^3F_2$	0	25	0	1	0	0	0	0	0	0
	1	$^3F_3$	9 786	9	30	2	−374	29	9 738	9 780	9 745	41
	2	$^3F_4$	18 564	18	50	1	−655	57	18 507	18 563	18 480	84
	3	$^3P_0$					−87	0	23 642	22 649		
	4	$^1D_2$	24 838	6	25	2	−355	29	25 285	24 835	24 320	518
	5	$^3P_1$					−238	29	28 750	27 905		
	6	$^3P_2$	39 044	8	30	2	−425	57	39 636	39 042	38 370	674
	7	$^1G_4$	39 718	36	44	1	−983	29	39 381	39 715	38 830	888
	8	$^1S_0$					−381	57	83 202	80 700		
$13+\ 4d^1$	0	$^2D_{3/2}$	0				0	0	0	0	0	0
	1	$^2D_{5/2}$	13 179				−439	30	13 144	12 740	13 212	−33
$14+\ 4p^6$	0	$^1S_0$					0	0	−540 785	−539 447		
$4p^5\ 4d^1$	1	$^3P_0$					−870	−128	−8 962	−8 970		
	2	$^3P_1$	0	11	0	2	−1 054	−128	0	0		
	3	$^3P_2$	17 311	12	12	2	−1 262	−97	17 544	17 392		
	4	$^3F_3$	19 275	40	50	1	−1 048	−128	19 247	19 115		
	5	$^3F_4$					−1 464	−97	21 027	20 991		
	6	$^1D_2$	30 278	16	30	2	−1 197	−128	30 252	31 345		
	7	$^3D_3$	50 891	16	30	2	−1 410	−97	51 770	51 208		
	8	$^3D_1$					−1 535	12	76 730	77 445		
	9	$^3F_2$					−1 996	12	91 543	93 484		
	10	$^3D_2$					−2 348	46	109 202	110 507		
	11	$^1F_3$					−2 445	46	117 668	118 362		
	12	$^1P_1$					−1 853	12	209 573	222 563		

Many of the identified levels are connected by Ritz combinations within the experimental uncertainty (red arrows in Fig. 1), enabling the sensitive verification of our $M1$ line identifications. Transitions shown by black arrows in Fig. 1 are not supported by Ritz combinations but there is no obvious other choice for their identification. The branching ratios obtained from the signal intensities can be compared to the gA predictions from the COWAN code. Agreement is found within a factor of two except for short wavelength lines at 275.6 and 291.2 nm, as is to be expected taking into account

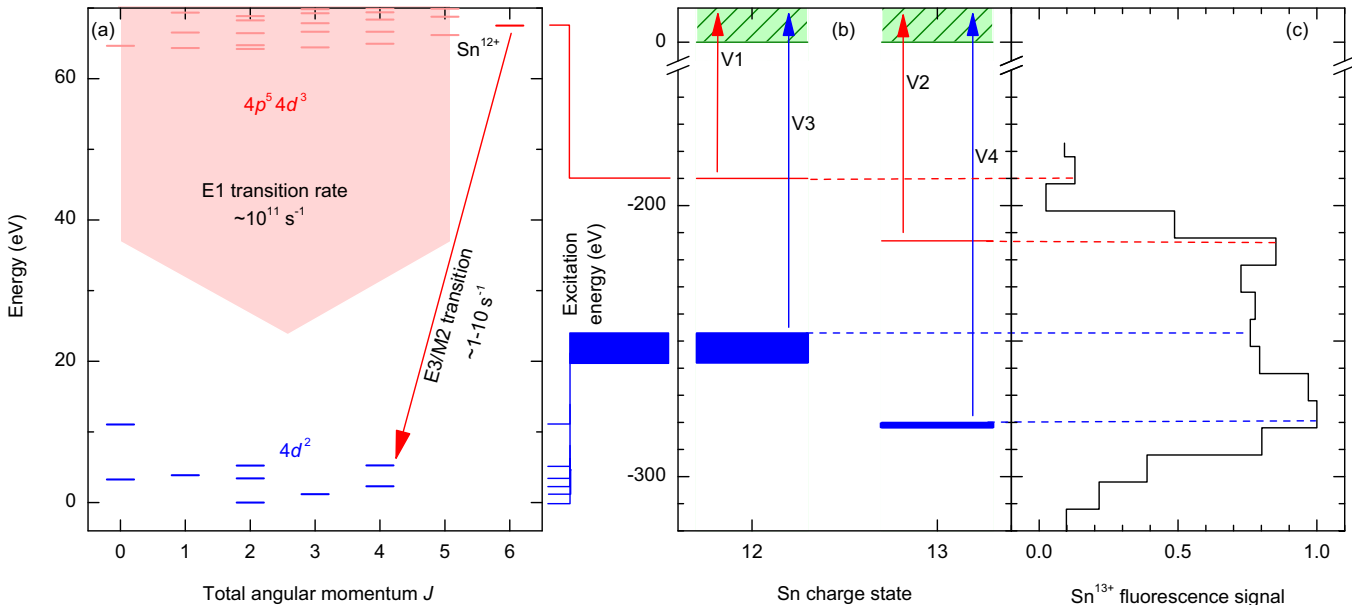

FIG. 4. Effect of metastable states on the in-EBIT production and fluorescence of Sn^{13+} from the ionization step $Sn^{12+} \rightarrow Sn^{13+}$. (a) Grotrian diagram of Sn^{12+}. States in the excited $4p^5\,4d^3$ and $4p^6\,4d^1\,4f^1$ configurations (light red) with total angular momenta $J \leqslant 5$ decay to the ground-state configuration $4p^6\,4d^2$ (blue) through fast $E1$ transitions. States with $J \geqslant 6$ are metastable (red) since all possible transitions require a change $\Delta J \geqslant 2$, and thus accumulate population. (b) The lowest such metastable states for Sn^{11+}–Sn^{14+} ions are ~60 eV closer to the continuum (green) than their ground states (blue). This allows ionization at an energy $V1$ that is lower than the corresponding ionization potential $V3$ for the ground state. Between $V1$ and $V3$, the value of $V2$ indicates the ionization threshold for metastable states of the fluorescing Sn^{13+} at which production of Sn^{14+} starts. For the Sn^{11+}–Sn^{14+} ions, the difference in (ground-state) ionization energies (~30 eV) is roughly only half as large as typical metastable-state energies (~60 eV). At the threshold $V4$, Sn^{13+} will be ionized from its ground state, and its population will decrease again. (c) The dependence of the Sn^{13+} fluorescence intensity (black curve) on the electron beam energy qualitatively follows this scenario. The electron beam energy [y axis in (c)] has been shifted by −20 eV (compare Fig. 3) to account for the electron beam space charge potential.

the experimental uncertainties including those related to the drop of spectrometer efficiency at short wavelengths.

The last column of Table III shows the differences between the level energies obtained in this work and those from the study of the EUV spectrum in Ref. [9]. The magnitude of the differences indicates that the analysis of EUV transitions in Ref. [9] needs to be revised.

2. Sn^{12+}

We find a very good agreement of our *ab initio* FSCC predictions with the experimental data for the five relatively strong transitions found in this work. In order to confirm this outcome, we compare them with earlier work.

All levels of the $4d^2$ ground configuration of Sn^{12+} were obtained previously in the analysis of EUV lines in discharge spectra [7]. Subsequent studies of the spectra of the Rh^{7+}, Pd^{8+}, Ag^{9+}, and Cd^{10+} ions from the Sn^{12+} isoelectronic sequence and the extrapolation of the isoelectronic regularities to Sn^{12+} showed [28], however, that the analysis in Ref. [7] of Sn^{12+} should be corrected.

In Fig. 6, the ratios of the energy parameters obtained from fits (FIT) and the *ab initio* Hartree-Fock values (HFR) of the electrostatic and spin-orbit parameters for the $[Kr]4d^2$ configuration in the aforementioned isoelectronic sequence [28] are shown. The points for Sn^{12+} were obtained by linear extrapolation of the data. The thus-obtained scaling factors for the electrostatic parameter F^4 and for the spin-orbit parameter, respectively, 0.897 and 1.027, are in close agreement with the values 0.900 and 1.030 obtained in Ref. [7]. However, the scaling factor for the electrostatic parameter F^2, at 0.850, disagrees with the value of 0.829 from Ref. [7]. The initial COWAN code calculations of energy levels, wavelengths, and transition probabilities for $M1$ transitions in this work were performed using the empirical scaling factors obtained from the mentioned extrapolation and taking $\alpha = 55$. These prior parameters enabled an accurate prediction of the Sn^{12+} level energies and enabled also the identification of all observed lines for this charge state. This strengthens our assignments of *ab initio* FSCC results to the observed transitions. The branching ratios of the intensity I of the identified transitions $I(4–6)$ and $I(1–6)$, as well as $I(1–7)$ and $I(2–7)$ (see Fig. 5) can be compared with predictions. The experimental ratio $I(4–6)/I(1–6) = 2.6$ is in agreement with the value 1.7 from the gA values obtained from COWAN calculations, given the uncertainty in the measurement of the total signal strength. Experimentally, we find $I(1–7)/I(2–7) = 1.3$, compared to the 1.8 from Cowan's theory. One Ritz combination is found, further confirming our identifications of the lines involved. The energy levels of Sn^{12+} derived from the wavelengths of Table I and optimized with the LOPT [43] code are collected in Table III. The magnitude of the differences between the here-obtained energy levels and the previously available experimental data [7] indicates that the identification of EUV transitions in that work needs to be revisited.

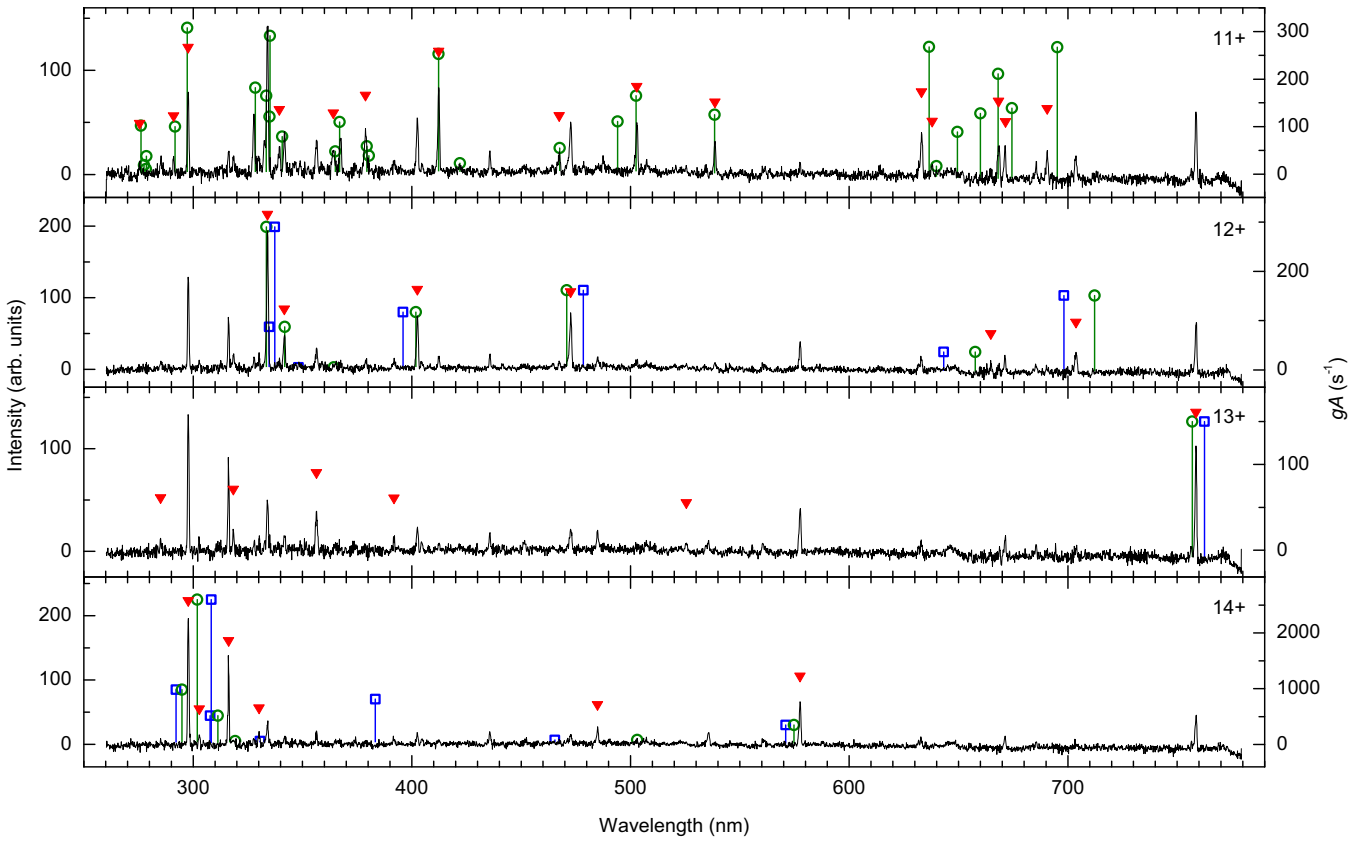

FIG. 5. Spectra of the charge states Sn^{11+}–Sn^{14+} (orange lines in Fig. 2). Signal intensities here are not corrected for instrument sensitivity. Lines marked with red full triangles belong to the respective charge state. Blue open squares: FSCC predictions. Green circles: semiempirical COWAN code calculations (see main text). The weighted transition rates gA are obtained from the COWAN code; they give a measure of the line strength of both theory predictions (right-hand y axis).

A comparison of the energy parameters is presented in Table II: those obtained from *ab initio* HFR calculations and those obtained from the final fitting of the COWAN code to the experimental level values obtained from LOPT. The scaling factors for the Sn^{12+} energy parameters are in agreement with the extrapolated values within the uncertainty of extrapolation. The trends in the change of the scaling factors from Sn^{12+} to Sn^{11+} can be used in extrapolation to the spectrum of Sn^{10+} for a better prediction of its $M1$ transitions; this is part of future work.

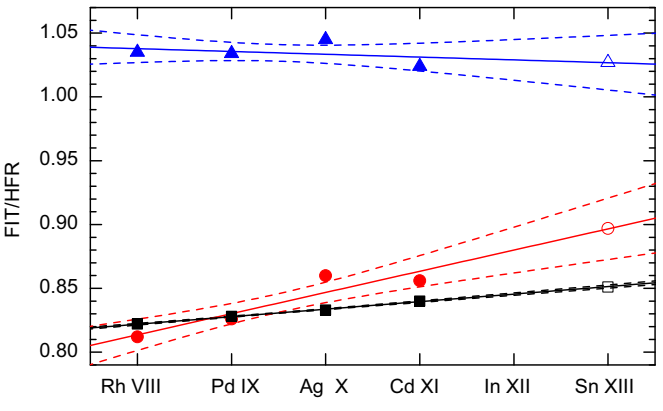

FIG. 6. Empirical adjustments of scaling factors in the COWAN code calculations: The ratios (FIT/HFR) for the electrostatic parameters F^2 (black squares) and F^4 (red circles), and for the spin-orbit parameter ζ (blue triangles) were obtained by fitting (FIT) to available data [28] and *ab initio* (HFR) COWAN values of the $[Kr]4d^2$ configuration in Rh^{7+}–Cd^{10+}. Solid lines represent linear fits and their extrapolation to Sn^{12+} (open symbols). Dashed lines delimit their 1-σ confidence bands.

3. Sn^{13+}

The *ab initio* FSCC calculations predicting a transition energy of 13 144 cm^{-1} for the $4d\ ^2D_{3/2}$–$^2D_{5/2}$ fine structure splitting are in good agreement with the line measured at 758.8(4)-nm wavelength, or 13 179(8) cm^{-1}. The data are also in excellent agreement with the result of 13 212(25) cm^{-1} given by Refs. [7,8]. This allowed us to use this line for unequivocally identifying the Sn^{13+} charge state. After correcting for the grating efficiency, this line is by far the brightest one observed in our measurements. Features at shorter wavelengths having low intensities stem from transitions between excited, densely packed states within the $[Ar]3d^{10}4s^24p^54d^2$ configuration. Identification of these transitions is outside the scope of this work.

4. Sn^{14+}

The [Kr] ground state configuration $4p^6\ ^1S_0$ does not exhibit a fine structure splitting and all contributions to the observed optical spectrum have to come from excited configurations, such as $[Ar]3d^{10}\ 4s^2\ 4p^5\ 4d^1$. All levels of this configuration

except the $J = 1$ levels are metastable for $E1$ transitions. The metastable states can thus decay and be observed through $M1$ fine-structure transitions. Identification of the observed optical lines was performed with the aid of the FSCC and COWAN code calculations. For the latter ones the Slater F^k and G^k parameters were scaled down to 90% of their *ab initio* values. The spin-orbit parameters for the $4p$ and $4d$ electrons were scaled by the factors 1.024 and 1.03, respectively: For the $4p$ electron we took a value evaluated for the $4p^5$ configuration in Sn^{15+} [45]; the value for the $4d$ electron was extrapolated from the spectra of Sn^{7+} [4], Sn^{11+} (see the previous section), and Sn^{12+} [7]. Additionally, the average energy of the configuration was adjusted so that the $^3D_1$ value 616 892 cm^{-1} obtained in the previous experiment [11] was reproduced exactly. The results of the calculations are shown in Table III along with the results of the FSCC calculations. There is good agreement between the wavelengths calculated by these two methods. We used the gA coefficients as obtained from the COWAN code.

As before, if we associate each predicted transition with the closest-lying, brightest transition, we find that all observed lines can be identified (see Table I). Moreover, if we now consider the fact that four of the transitions identified here form a Ritz group (see Fig. 1), we obtain a sensitive tool for checking our tentative assignments. Indeed, the assigned spectral lines form such a group well within the experimental uncertainty. The poor agreement between the experimental and theoretical branching ratio $I(3–7)/I(6–7)$ could well be related to the poorer agreement between theory and experiment regarding the wavelengths of the assigned transitions. This discrepancy indicates an inaccurate determination of the involved wave functions and, hence, of gA coefficients. Furthermore, as discussed in the case of Sn^{11+}, experimental uncertainties in the determination of the signal intensity increase for short wavelengths like that of the 3–7 transition used in the comparison above.

The identification of the line at 316.3 nm is achieved considering that the branching ratio $I(3–7)/I(4–7) \approx 2$ fits best by assigning this line to the 4–7 transition. There appears to be no other choice for the weak line at 302.9 nm but the 8–10 transition even though the gA value for this transition is the largest of all predicted transitions. It should be noted that another predicted transition with large gA, namely 9–11, is absent from the spectrum. Both transitions start from high-lying levels and the apparent low intensities of the corresponding lines could be explained by a lower population of these levels. The experimental fine structure splittings E_{exp} of the $4p^5\,4d^1$ configuration, given in Table III, were obtained by inserting the wavelengths of the transitions identified here into LOPT, keeping the $^3P_1$ level fixed at the Hartree-Fock value. The agreement of *ab initio* FSCC and the semiempirical COWAN results with experimental data in Table III is excellent. The *ab initio* FSCC method performs at the same level of accuracy as semiempirical Cowan code that uses extensive input data. Furthermore, agreement of FSCC predictions of the energy of the levels 8 ($^3D_1$ at 617 515 cm^{-1}) and 12 ($^1P_1$ at 750 358 cm^{-1}) with previous experimental work in the EUV [11], which yielded 616 892 and 749 429 cm^{-1}, respectively, is outstanding.

Transitions in the EUV stemming from the configurations $4p^5\,4d^1$–$4p^5\,5p^1$ were observed previously [14]. In that work, several peaks in the recorded spectrum were assigned using COWAN code calculations but level energies were not derived because of poor resolution and strong overlap of the various lines. However, there are several cases when two EUV lines starting from the same $4p^5\,5p^1$ level were measured. Thereby, the separation between the $4p^5\,4d^1$ levels was found and compared to the levels given in Table III. The splittings $^3P_2$–$^3D_3$ and $^3F_3$–$^1D_2$ are 33 600(1 500) and 11 100(1 500) cm^{-1}, respectively. Our values for these intervals, respectively 33 580(20) and 11 003(43) cm^{-1}, are in good agreement. Therefore, the uncertainty of the relative wavelengths in Ref. [14] might be better than the quoted 0.02 nm, a finding that also supports our identification of the visible EBIT lines.

V. CONCLUSIONS

We have re-evaluated the fine structure of Sn^{11+}–Sn^{14+} ions, which are of particular interest for EUV plasma light sources used in next-generation nanolithography. Experimentally, we combined optical spectroscopy of magnetic dipole $M1$ transitions with charge-state selective ionization in an EBIT. The registered optical spectra were analyzed and line identifications were obtained based on *ab initio* FSCC calculations as well as semi-empirical COWAN code calculations that had adjustable parameters allowing us to fit the observed spectra. Both the FSCC calculations and the semiempirical COWAN calculations showed good agreement. The present measurements and identifications provide immediate input for optical plasma-diagnostic tools. Furthermore, our identifications of transitions confirm the very good predictive power of *ab initio* FSCC calculations. Given these encouraging results, it would be particularly advantageous if FSCC could be further developed, as in the current state of the code only atomic systems with a maximum of two open-shell electrons or holes can be treated. Comparison of our results with previous work suggests that line identifications based on EUV data need to be revisited. In this type of complex correlated electronic systems, optical spectroscopy delivers data that both complements and challenges studies in the EUV regime and their interpretations.

[1] J. Benschop, V. Banine, S. Lok, and E. Loopstra, J. Vac. Sci. Technol. B **26**, 2204 (2008).
[2] V. Y. Banine, K. N. Koshelev, and G. H. P. M. Swinkels, J. Phys. D: Appl. Phys. **44**, 253001 (2011).
[3] G. O'Sullivan, B. Li, R. D'Arcy, P. Dunne, P. Hayden, D. Kilbane, T. McCormack, H. Ohashi, F. O'Reilly, P. Sheridan, E. Sokell, C. Suzuki, and T. Higashiguchi, J. Phys. B **48**, 144025 (2015).
[4] V. I. Azarov and Y. N. Joshi, J. Phys. B **26**, 3495 (1993).
[5] I. Y. Tolstikhina, S. S. Churilov, A. N. Ryabtsev, and K. N. Koshelev, in *EUV Sources for Lithography*, edited by V. Bakshi (SPIE Press, Bellingham, Washington, 2006), Vol. 149, p. 113.

[6] S. S. Churilov and A. N. Ryabtsev, Opt. Spectrosc. **100**, 660 (2006).

[7] S. S. Churilov and A. N. Ryabtsev, Opt. Spectrosc. **101**, 169 (2006).

[8] A. N. Ryabtsev, É. Y. Kononov, and S. S. Churilov, Opt. Spectrosc. **105**, 844 (2008).

[9] S. S. Churilov and A. N. Ryabtsev, Phys. Scr. **73**, 614 (2006).

[10] W. Svendsen and G. O'Sullivan, Phys. Rev. A **50**, 3710 (1994).

[11] J. Sugar, W. L. Rowan, and V. Kaufman, JOSA B **8**, 2026 (1991).

[12] J. Sugar, W. L. Rowan, and V. Kaufman, JOSA B **9**, 1959 (1992).

[13] H. Ohashi, S. Suda, H. Tanuma, S. Fujioka, H. Nishimura, K. Nishihara, T. Kai, A. Sasaki, H. A. Sakaue, N. Nakamura *et al.*, J. Phys.: Conf. Ser. **163**, 012071 (2009).

[14] R. D'Arcy, H. Ohashi, S. Suda, H. Tanuma, S. Fujioka, H. Nishimura, K. Nishihara, C. Suzuki, T. Kato, F. Koike, J. White, and G. O'Sullivan, Phys. Rev. A **79**, 042509 (2009).

[15] R. D'Arcy, H. Ohashi, S. Suda, H. Tanuma, S. Fujioka, H. Nishimura, K. Nishihara, C. Suzuki, T. Kato, F. Koike, A. O'Connor, and G. O'Sullivan, J. Phys. B **42**, 165207 (2009).

[16] H. Ohashi, S. Suda, H. Tanuma, S. Fujioka, H. Nishimura, A. Sasaki, and K. Nishihara, J. Phys. B **43**, 065204 (2010).

[17] J. Yatsurugi, E. Watanabe, H. Ohashi, H. A. Sakaue, and N. Nakamura, Phys. Scr. **T144**, 014031 (2011).

[18] M. F. Gu, Can. J. Phys. **86**, 675 (2008).

[19] S. W. Epp, J. R. Crespo López-Urrutia, M. C. Simon, T. Baumann, G. Brenner, R. Ginzel, N. Guerassimova, V. Mäckel, P. H. Mokler, B. L. Schmitt *et al.*, J. Phys. B **43**, 194008 (2010).

[20] E. Eliav, U. Kaldor, and Y. Ishikawa, Phys. Rev. A **49**, 1724 (1994).

[21] E. Eliav, U. Kaldor, and Y. Ishikawa, Phys. Rev. A **50**, 1121 (1994).

[22] R. D. Cowan, *The Theory of Atomic Structure and Spectra* (University of California Press, Berkeley, Los Angeles, London, 1981); available online, e.g., at http://das101.isan.troitsk.ru/cowan.htm, modified by A. Kramida.

[23] I. Lindgren, Int. J. Quantum Chem. **57**, 683 (1996).

[24] E. Eliav, U. Kaldor, and Y. Ishikawa, Phys. Rev. A **51**, 225 (1995).

[25] D. K. Nandy and B. K. Sahoo, Phys. Rev. A **88**, 052512 (2013).

[26] M. S. Safronova, V. A. Dzuba, V. V. Flambaum, U. I. Safronova, S. G. Porsev, and M. G. Kozlov, Phys. Rev. Lett. **113**, 030801 (2014).

[27] A. Windberger, J. R. Crespo López-Urrutia, H. Bekker, N. S. Oreshkina, J. C. Berengut, V. Bock, A. Borschevsky, V. A. Dzuba, E. Eliav, Z. Harman, U. Kaldor, S. Kaul, U. I. Safronova, V. V. Flambaum, C. H. Keitel, P. O. Schmidt, J. Ullrich, and O. O. Versolato, Phys. Rev. Lett. **114**, 150801 (2015).

[28] A. N. Ryabtsev and E. Y. Kononov, Phys. Scr. **84**, 015301 (2011).

[29] B. M. Penetrante, J. N. Bardsley, D. DeWitt, M. Clark, and D. Schneider, Phys. Rev. A **43**, 4861 (1991).

[30] G. Brenner, J. R. Crespo López-Urrutia, Z. Harman, P. H. Mokler, and J. Ullrich, Phys. Rev. A **75**, 032504 (2007).

[31] H. Bekker, O. O. Versolato, A. Windberger, N. S. Oreshkina, R. Schupp, T. M. Baumann, Z. Harman, C. H. Keitel, P. O. Schmidt, J. Ullrich, and J. R. Crespo López-Urrutia, J. Phys. B **48**, 144018 (2015).

[32] G. C. Rodrigues, P. Indelicato, J. P. Santos, P. Patté, and F. Parente, At. Data. Nucl. Data Tables **86**, 117 (2004).

[33] A. Kramida, Yu. Ralchenko, J. Reader, and NIST ASD Team, NIST Atomic Spectra Database (ver. 5.3), http://physics.nist.gov/asd (National Institute of Standards and Technology, Gaithersburg, MD, 2015).

[34] J. Sucher, Phys. Rev. A **22**, 348 (1980).

[35] Y. Ishikawa, R. Baretty, and R. C. Binning, Chem. Phys. Lett. **121**, 130 (1985).

[36] E. Eliav, M. J. Vilkas, Y. Ishikawa, and U. Kaldor, J. Chem. Phys. **122**, 224113 (2005).

[37] G. L. Malli, A. B. F. Da Silva, and Y. Ishikawa, Phys. Rev. A **47**, 143 (1993).

[38] TRAFS-3C code (Tel Aviv Relativistic Atomic Fock-Space Coupled Cluster code), written by E. Eliav, U. Kaldor, and Y. Ishikawa (1990–2013), with contributions by A. Landau.

[39] V. M. Shabaev, I. I. Tupitsyn, and V. A. Yerokhin, Comput. Phys. Commun. **189**, 175 (2015).

[40] J. R. Crespo López-Urrutia, P. Beiersdorfer, K. Widmann, and V. Decaux, Can. J. Phys. **80**, 1687 (2002).

[41] Y. Kobayashi, K. Kubota, K. Omote, A. Komatsu, J. Sakoda, M. Minoshima, D. Kato, J. Li, H. A. Sakaue, I. Murakami *et al.*, Phys. Rev. A **92**, 022510 (2015).

[42] A. Borovik, Jr., M. F. Gharaibeh, P. M. Hillenbrand, S. Schippers, and A. Müller, J. Phys. B **46**, 175201 (2013).

[43] A. E. Kramida, Comput. Phys. Commun. **182**, 419 (2010).

[44] A. N. Ryabtsev and E. Y. Kononov, Phys. Scr. **91**, 025402 (2016).

[45] E. Biémont, R. D. Cowan, and J. E. Hansen, Phys. Scr. **37**, 850 (1988).